

Lens modelling of the strongly lensed Type Ia supernova iPTF16geu

E. Mörtzell,¹★ J. Johansson,² S. Dhawan,¹ A. Goobar^{1b},¹ R. Amanullah¹
and D. A. Goldstein³†

¹*Oskar Klein Centre, Department of Physics, Stockholm University, SE-106 91 Stockholm, Sweden*

²*Department of Physics and Astronomy, Division of Astronomy and Space Physics, Uppsala University, Box 516, SE-751 20 Uppsala, Sweden*

³*Division of Physics, Mathematics and Astronomy, California Institute of Technology, Pasadena, CA 91125, USA*

Accepted 2020 June 2. Received 2020 May 8; in original form 2019 July 15

ABSTRACT

In 2016, the first strongly lensed Type Ia supernova (SN Ia), iPTF16geu, at redshift $z = 0.409$ with four resolved images arranged symmetrically around the lens galaxy at $z = 0.2163$, was discovered. Here, refined observations of iPTF16geu, including the time delay between images, are used to decrease uncertainties in the lens model, including the the slope of the projected surface density of the lens galaxy, $\Sigma \propto r^{1-\eta}$, and to constrain the universal expansion rate H_0 . Imaging with *Hubble Space Telescope* provides an upper limit on the slope η , in slight tension with the steeper density profiles indicated by imaging with Keck after iPTF16geu had faded, potentially due to dust extinction not corrected for in host galaxy imaging. Since smaller η implies larger magnifications, we take advantage of the standard candle nature of SNe Ia constraining the image magnifications, to obtain an independent constraint of the slope. We find that a smooth lens density fails to explain the iPTF16geu fluxes, regardless of the slope, and additional substructure lensing is needed. The total probability for the smooth halo model combined with star microlensing to explain the iPTF16geu image fluxes is maximized at 12 per cent for $\eta \sim 1.8$, in excellent agreement with Keck high-spatial-resolution data, and flatter than an isothermal halo. It also agrees perfectly with independent constraints on the slope from lens velocity dispersion measurements. Combining with the observed time delays between the images, we infer a lower bound on the *Hubble* constant, $H_0 \gtrsim 40 \text{ km s}^{-1} \text{ Mpc}^{-1}$, at 68.3 per cent confidence level.

Key words: gravitational lensing: strong – gravitational lensing: micro – supernovae: individual – distance scale.

1 INTRODUCTION

The expansion history of the Universe can be constrained by measuring redshifts and distances of standard candles such as Type Ia supernovae (SNe Ia; Goobar & Leibundgut 2011). The redshift gives the growth since the time when the light was emitted. This time is measured, together with the spatial curvature of the Universe, by the distance to the SNe Ia as inferred from its apparent magnitude.

Weak gravitational lensing from inhomogeneities in the matter distribution will cause a scatter in the distance measurements, possibly degrading the accuracy of the cosmological parameters derived from the expansion history. The first tentative detection of the gravitational magnification of SNe Ia was made in Jönsson et al. (2007); see also Mörtzell, Gunnarsson & Goobar (2001b),

Jönsson et al. (2006), Nordin et al. (2014), Rodney et al. (2015), and Rubin et al. (2018). In principle, the effect can be corrected for by cross-correlating the SNe Ia observations with data on the foreground galaxies responsible for the lensing effect (Amanullah, Mörtzell & Goobar 2003; Jönsson et al. 2006, 2008; Jönsson, Mörtzell & Sollerman 2009). The induced scatter can also be used to measure the masses of the foreground galaxies (Jönsson et al. 2010) and to constrain the fraction of matter inhomogeneities in compact objects (Rauch 1991; Metcalf & Silk 1999; Seljak & Holz 1999; Goliath & Mörtzell 2000; Mörtzell, Goobar & Bergstrom 2001a; Mörtzell 2002; Zumalacarregui & Seljak 2018); see also Dhawan, Goobar & Mörtzell (2018).

In this paper, we study the first resolved strongly lensed SNe Ia. It is well known that the time delay between images in strong gravitational lensing systems can be used to constrain the *Hubble*

* E-mail: edvard@fysik.su.se

† Hubble Fellow.

constant, H_0 (Refsdal 1964); see also Goobar et al. (2002), Mörtzell, Dahle & Hannestad (2005), and Mörtzell & Sunesson (2006). SNe Ia are especially useful in this respect because of the following (Kolatt & Bartelmann 1998; Oguri & Kawano 2003):

- (i) The time delay can potentially be measured with high accuracy.
- (ii) Their standard candle nature can partly break the mass and source sheet degeneracy.
- (iii) Their transient nature allows for accurate reference imaging.

Given the persistent tension (currently at the 4.4σ level; Riess et al. 2019) between H_0 inferred from local distance indicators and the cosmic microwave background (CMB; Aghanim et al. 2016), independent measurements of the current expansion rate will shed light on possible explanations (e.g. Mörtzell & Dhawan 2018).

The first observed SN Ia with expected multiple images is PS1-10afx at redshift $z = 1.388$ and a flux magnification $\mu \sim 30$ (Chornock et al. 2013; Quimby et al. 2013). However, the strong lensing nature of the system was not verified by high spatial resolution imaging.

Searches for high-redshift core-collapse SNe, intrinsically fainter than SNe Ia, has profited from observations through lensing clusters of galaxies (Goobar et al. 2009; Amanullah et al. 2011; Petrushevska et al. 2016). Four images of the core-collapse SN Refsdal at $z = 1.49$ were also observed in the line of sight of a massive cluster (Kelly et al. 2016b). Lens models of the cluster predicted that a fifth image should reappear within 500 d, in agreement with the subsequent detection of the image after 310–380 d (Kelly et al. 2016a). Unlike SNe Ia, lensed core-collapse SNe can not be used to measure the lensing magnification directly.

The first strongly lensed SN Ia, iPTF16geu at redshift $z = 0.409$, was identified by its high magnification $\mu > 50$ (Goobar et al. 2017). Subsequent high-spatial-resolution imaging confirmed the multiple images of the SNe Ia. In Goobar et al. (2017), the positions of the SN images with respect to the lensing galaxy were used to construct a lensing model, an isothermal ellipsoid galaxy (Kassiola & Kovner 1993; Kormann, Schneider & Bartelmann 1994) with ellipticity $\epsilon_e = 0.15 \pm 0.07$ and mass $M = (1.70 \pm 0.06) \times 10^{10} M_\odot$ within a radius of ~ 1 kpc. The total magnification of the SN images was not well constrained by the model, but the adopted smooth lens halo predicted brightness differences between the SN images in disagreement with observations, providing evidence for substructures in the lensing galaxy, possibly in the forms of stars. The time delays between images were predicted to be shorter than 35 h at 99.9 per cent confidence level (CL). The system was also studied in More et al. (2017) where the anomalous image flux ratios were confirmed and time delays between images were predicted to be less than a day. Also, the slope of the lens mass distribution was constrained to be $\eta = 2.1 \pm 0.1$, consistent with an isothermal profile for which $\eta = 2$. In Yahalomi, Schechter & Wambsganss (2017), anomalies between macro-model predictions and the observed iPTF16geu flux ratios were investigated, finding that the discrepancies are too large to be due to microlensing alone. Using the macrolens models from More et al. (2017), the probability for microlensing to explain the observed flux ratio was found to be 0.3 per cent. Allowing for alternative macromodels, with varying contributions from external shear and ellipticity, increased the probability to 3 per cent.

Substantial effort in obtaining follow-up data, including reference imaging after iPTF16geu had faded, has resulted in smaller uncertainties in SN image positions and lens galaxy properties, as well as the first observational constraints on the time delay between

SN images, as presented in an accompanying paper (Dhawan et al. 2020), summarized in Section 4.

In this paper, we take advantage of the better observational constraints on the system to refine the lens model and investigate the dependence on the expansion rate H_0 . We also quantify to what degree lens galaxy stellar microlensing can explain the observed image flux anomalies taking the new data into account.

We use geometrized units for which $c = G = 1$ and express the dimensionless *Hubble* constant, h , in units of $100 \text{ km s}^{-1} \text{ Mpc}^{-1}$:

$$h \equiv \frac{H_0}{100 \text{ km s}^{-1} \text{ Mpc}^{-1}}. \quad (1)$$

2 GRAVITATIONAL LENSING

When light from a source at angular position β and redshift z_s passes a mass at z_l along its path, it is deflected and observed at an angle θ . The time delay, Δt , compared to an unlensed image is given by

$$\Delta t = \frac{D_s D_l}{D_{ls}} (1 + z_l) \tau, \quad \tau \equiv \frac{1}{2} (\theta - \beta)^2 - \Psi(\theta), \quad (2)$$

where the combination,

$$D_{\Delta t} \equiv \frac{D_s D_l}{D_{ls}} (1 + z_l), \quad (3)$$

is denoted the time delay distance. Here, D_l , D_s , and D_{ls} are angular distances to the lens, source, and between the lens and source, respectively, and $\Psi(\theta)$ is the scaled, projected Newtonian potential, Φ , of the lens,

$$\Psi(\theta) = 2 \frac{D_{ls}}{D_s D_l} \int \Phi dl, \quad (4)$$

integrated along the path of the light ray. It is related to the surface mass density of the lens, or convergence through the Poisson equation, $\kappa = \nabla^2 \Psi / 2$, giving

$$\kappa(\theta) = 4\pi \frac{D_l D_{ls}}{D_s} \int \rho dl = \frac{\Sigma(\theta)}{\Sigma_{\text{crit}}}, \quad (5)$$

where

$$\Sigma(\theta) \equiv \int \rho dl \quad \text{and} \quad \Sigma_{\text{crit}} \equiv \frac{1}{4\pi} \frac{D_s}{D_l D_{ls}}. \quad (6)$$

Using Fermat's principle that light rays traverse paths of stationary time with respect to variations of the path, we obtain the lens equation:

$$\beta = \theta - \alpha(\theta), \quad (7)$$

where $\alpha(\theta) = \nabla \Psi(\theta)$. Given the Jacobian matrix of the lens mapping,

$$\mathcal{A}(\theta) = \frac{\delta \beta}{\delta \theta}, \quad (8)$$

the magnification, $\mu(\theta)$, is given by

$$\mu(\theta) = \frac{1}{\det \mathcal{A}(\theta)} = \frac{1}{(1 - \kappa)^2 - \gamma^2}, \quad (9)$$

where the shear $\gamma = \sqrt{\gamma_1^2 + \gamma_2^2}$ and (here, subscripts denote partial derivatives with respect to angle components θ_i)

$$\gamma_1 = \frac{1}{2} (\Psi_{11} - \Psi_{22}), \quad \gamma_2 = \Psi_{12} = \Psi_{21}. \quad (10)$$

2.1 Mass sheet degeneracy

If we rescale Ψ using the scalars ξ and u , and the vector s as

$$\Psi' = \xi\Psi + \frac{1-\xi}{2}\theta^2 + s \cdot \theta + u, \quad (11)$$

the deflection angle $\alpha = \nabla\Psi$ rescales as

$$\alpha' = \xi\alpha + (1-\xi)\theta + s, \quad (12)$$

and the convergence according to

$$1 - \kappa' = \xi(1 - \kappa). \quad (13)$$

If we also rescale the (unobserved) source position $\beta' = \xi\beta - s$, the image positions will be unchanged. This is the mass sheet degeneracy; given only the observed image positions, we are free to rescale the projected mass.¹ Magnification and time delay predictions, however, will change according to

$$\mu' = \frac{\mu}{\xi^2} \quad \text{and} \quad \Delta t' = \xi \Delta t. \quad (14)$$

From equation (2), the inferred h is proportional to the predicted $\Delta t'$ from the lens model, $h' = \xi h$. Error propagation gives

$$\begin{aligned} \frac{\delta\mu'}{\mu'} &= -2\frac{\delta\xi}{\xi}, \\ \frac{\delta h'}{h'} &= \frac{\delta\xi}{\xi} = -\frac{\delta\mu}{2\mu} \approx -0.46\delta(\Delta m), \end{aligned} \quad (15)$$

where Δm is the magnification expressed in magnitudes. For an SN Ia, $|\Delta m| \approx 0.1$, and the fractional uncertainty on h from the mass sheet degeneracy is of the order of 5 per cent, ignoring additional substructure magnifications; see Section 8.3.

3 LENS MODEL

For a cored isothermal ellipsoid, the convergence is given by (Kassiola & Kovner 1993; Kormann et al. 1994)

$$\kappa = \frac{b}{2\sqrt{s^2 + (1-\epsilon)\theta_1^2 + (1+\epsilon)\theta_2^2}}, \quad (16)$$

where b is a mass normalization corresponding to the Einstein radius θ_E for $s = 0$, s is the core radius, and ϵ is related to the minor and major axial ratio q as

$$q^2 = \frac{1-\epsilon}{1+\epsilon}. \quad (17)$$

In terms of the ellipticity, ϵ_e , and eccentricity, e ,

$$\begin{aligned} \epsilon_e &= 1 - q = 1 - \sqrt{\frac{1-\epsilon}{1+\epsilon}}, \\ e &= \sqrt{1 - q^2} = \sqrt{\frac{2\epsilon}{1+\epsilon}}. \end{aligned} \quad (18)$$

We can generalize equation (16) as

$$\kappa = \frac{b^{\eta-1}}{2[s^2 + (1-\epsilon)\theta_1^2 + (1+\epsilon)\theta_2^2]^{(\eta-1)/2}}, \quad (19)$$

for which $\theta_E = b\sqrt{(1+q^2)/2q}$. In the core-less circularly symmetric case ($\epsilon = s = 0$), equation (19) is a good approximation of the projection of a three-dimensional density profile $\rho \propto r^{-\eta}$, where

¹Possibly restricted by physical considerations, such as keeping the projected mass positive.

$r^2 = \theta_1^2 + \theta_2^2$, for $\eta = n$. For a singular isothermal sphere (SIS), $\epsilon = s = 0$ and $\eta = n = 2$. We refer to its elliptical generalization $\epsilon \neq 0$ as a singular isothermal ellipsoid (SIE). For an SIE lens, the image magnification and convergence are related by $\mu_{\text{SIE}} = (1 - 2\kappa_{\text{SIE}})^{-1}$.

In terms of the dimensionless τ , the time delay between two lensed images, I and II, of a single source is

$$\begin{aligned} \Delta\tau &= \tau_{\text{II}} - \tau_{\text{I}} = \frac{(\theta_{\text{II}} - \beta)^2}{2} - \Psi_{\text{II}} - \frac{(\theta_{\text{I}} - \beta)^2}{2} + \Psi_{\text{I}} \\ &= \frac{r_{\text{I}}^2 - r_{\text{II}}^2}{2} \left[1 + \frac{2(\theta_{\text{II}} \cdot \alpha_{\text{II}} - \theta_{\text{I}} \cdot \alpha_{\text{I}} + \Psi_{\text{I}} - \Psi_{\text{II}})}{r_{\text{I}}^2 - r_{\text{II}}^2} \right]. \end{aligned} \quad (20)$$

For a SIS halo, $\Psi = \theta \cdot \alpha$ and

$$\Delta\tau_{\text{SIS}} = \frac{r_{\text{I}}^2 - r_{\text{II}}^2}{2}. \quad (21)$$

Converting into polar coordinates, for two images on opposite sides of the lens, we can gain some analytical insight by Taylor expanding in (Mörtzell et al. 2005)

$$p \equiv \frac{\Delta r}{r} = \frac{2(r_{\text{I}} - r_{\text{II}})}{r_{\text{I}} + r_{\text{II}}} \quad \text{and} \quad \delta \equiv \phi_{\text{I}} + \pi - \phi_{\text{II}}, \quad (22)$$

obtaining

$$\Delta\tau = \Delta\tau_{\text{SIS}}(\eta - 1) \left[1 - \frac{(\eta - 2)^2}{12} p^2 - \frac{\eta - 2}{4} \delta^2 \right]. \quad (23)$$

For symmetric systems, like iPTF16geu, for which p and δ are small, the time delays are simply given by the difference of the squared image distances from the lens centre times a factor $(\eta - 1)/2$.

Note that the time delay only depends on the slope of the projected surface density at radii between the images (Falco, Gorenstein & Shapiro 1985). The main uncertainty affecting the precision of $\Delta\tau$, and thus h is usually the slope of the surface mass density, η , in the annulus between the images.

4 SUMMARY OF OBSERVATIONS

We here summarize the observations, and the derived characteristics of iPTF16geu, as described in more detail in Goobar et al. (2017) and Dhawan et al. (2020).

For the iPTF16geu lens system, the redshifts are $z_{\text{I}} = 0.2163$ and $z_{\text{s}} = 0.409$, corresponding to angular distances, assuming flat *Planck* parameter values of $h = 0.678$ and $\Omega_{\text{M}} = 0.308$ (Ade et al. 2016):

$$D_{\text{I}} = 745.8, \quad D_{\text{s}} = 1157.0 \quad \text{and} \quad D_{\text{Is}} = 513.2 \text{ Mpc.}$$

Expressing positions in arcseconds (arcsec), the time delay distance in equation (3) is given by (again assuming flat *Planck* parameter) $D_{\Delta t} = 57.27$ d.

The discovery of iPTF16geu prompted observations with the *Hubble Space Telescope* (*HST*) Wide Field Camera 3 using the ultraviolet and near-infrared (NIR) channels, as well as with laser guided star adaptive optics (LGS-AO) at the Very Large Telescope (VLT) and Keck (Goobar et al. 2017). Subsequent data, while iPTF16geu was active, were collected until it disappeared behind the Sun, as well as after it had faded below the detection limit using *HST* and LGS-AO NIR observations at the Keck telescope in *J*, *H*, and *K_s* bands. For *J* and *H*, we obtained nine exposures of 20 s each following a dithering pattern. For the *K_s* band, 18 exposures of 65 s were acquired (Dhawan et al. 2020). Together with the data presented in Goobar et al. (2017), this resulted in three epochs for *J* and two epochs for the *H* and *K_s* bands, respectively. The *HST* data are summarized in table 1 in Dhawan et al. (2020).

Table 1. Observed image positions, arrival times, and magnifications of iPTF16geu images (Dhawan et al. 2020).

Image	r (arcsec)	ϕ	t_{obs} (d)	μ_{obs}
1	0.251 ± 0.001	4.468 ± 0.002	0 ± 0.33	35.6 ± 1.1
2	0.324 ± 0.001	2.679 ± 0.003	-0.23 ± 0.99	15.7 ± 1.1
3	0.297 ± 0.002	1.013 ± 0.006	-1.43 ± 0.64	7.5 ± 1.1
4	0.276 ± 0.001	5.860 ± 0.005	1.36 ± 1.07	9.1 ± 1.1

Note. The radial coordinate is given in arcsec, the angle ϕ in radians north of east, and the time delay in days.

Table 2. Observed time delay differences, $\Delta t_{ij} \equiv t_j - t_i$, and magnification ratios, $r_{ij} \equiv \mu_i/\mu_j$, between iPTF16geu images.

Images (ij)	Δt_{ij} (d)	r_{ij}
12	0.23 ± 1.04	2.27 ± 0.17
13	1.43 ± 0.81	4.74 ± 0.74
14	-1.36 ± 1.12	3.91 ± 0.50

Multiband photometry for the resolved images of iPTF16geu is obtained using a combination of a forward modelling approach and template subtractions. The data described above are used to fit for the global light-curve parameters, including light-curve peak and shape, as well as colour excess from intrinsic colour variations or dimming by dust in the host galaxy. The light curves are also corrected for Milky Way dust. Additionally, the resolved images are used to fit for the time offsets between the four SN images, the SN image positions, as well as extinction in the lensing galaxy for each individual line of sight. Assuming a total-to-selective extinction ratio $R_V = A_V/E(B - V) = 2$ in the host and lens galaxies, we find $E(B - V)_{\text{host}} = 0.29 \pm 0.05$ mag (common for all images) and $E(B - V)_{\text{lens}}$ for images 1, 2, 3, and 4 of 0.06 ± 0.08 , 0.17 ± 0.08 , 0.42 ± 0.09 , and 0.94 ± 0.07 mag, respectively, showing that especially image 4 is heavily extinguished in the lens galaxy. Combining the intrinsic source luminosity standardized from the light-curve shapes and colours, with the light-curve peak heights and individual image dust extinctions, the magnification factor for each image can be computed.

The derived image positions, arrival times, and magnifications are constrained to the values given in Table 1 (Dhawan et al. 2020). The total magnification of iPTF16geu is $\mu_{\text{tot}} = 67.8^{+2.6}_{-2.9}$. The corresponding time delay differences, $\Delta t_{ij} \equiv t_j - t_i$, and magnification ratios, $r_{ij} \equiv \mu_i/\mu_j$, are presented in Table 2. The fact that data are consistent with zero time delay between images means that we can only hope to be able to put a lower limit on h .

5 MACROLENS IMAGE MODELLING

In this section, we constrain the parameters of the macrolens model given in equation (16) using imaging of the lens and host galaxy light distribution, as well as the iPTF16geu image positions. Here, the fluxes of the individual iPTF16geu image fluxes are not included in the fits. In subsequent sections, we also take advantage of the standard nature of the SN source to make use of the iPTF16geu image magnifications in the modelling procedure.

5.1 Lens mass constraints from iPTF16geu image positions

In line with the analysis in Goobar et al. (2017), we first use only the SN image positions to constrain the parameters of the lens mass model, including b , ϵ , the slope η , the core size s , the orientation of the major axis, the position of the centre of mass of the lensing galaxy, and the corresponding iPTF16geu source position,

employing the `lensmodel` software package (Keeton 2001a,b). Since the image fluxes can be subjected to systematics effects such as lensing by substructure and dust extinction not properly corrected for, this represents the most conservative approach to the problem.²

The slope and core size are not well constrained by the SN positions, since varying η and/or s can be compensated for by changing b in a way that keeps the total mass within the images constant. When varying the slope of the lens, flux ratios vary little, but the total magnification varies a lot. We can thus get a wide range of magnifications, even without invoking the mass sheet degeneracy.

At least, in principle, the central surface density can be constrained by the fact that we do not observe a central image of iPTF16geu. Close to the centre of the lens, the image magnification is given by

$$\mu_{\text{central}} \approx \frac{1}{(1 - \kappa)^2}. \quad (24)$$

If we can observationally constrain $\mu_{\text{central}} < \mu_{\text{max}}$, then (for $\kappa > 1$)

$$\kappa > 1 + \frac{1}{\sqrt{\mu_{\text{max}}}} \rightarrow \Sigma_{\text{central}} > \Sigma_{\text{crit}} \left(1 + \frac{1}{\sqrt{\mu_{\text{max}}}} \right), \quad (25)$$

where $\Sigma_{\text{crit}} \approx 10.50 \text{ kg m}^{-2}$ for iPTF16geu. Since we expect the central image to be subject to large dust extinction not accounted for in the analysis, equation (25) represents the most optimistic limit obtainable for the lens galaxy central surface density. Assuming a Hsiao template (Hsiao et al. 2007), with a Bessell B -band magnitude of -19.3 , reddened by $A_V = 0.23$ mag in the Milky Way and $A_V = 0.58$ mag in the host galaxy, the 3σ upper limit on a possible fifth central image corresponds to a demagnification of 1.2 mag, or $\mu_{\text{max}} = 0.33$, implying $\Sigma_{\text{central}} > 29 \text{ kg m}^{-2}$. At least, in principle, the lack of a detected central image can be used also to constrain the slope of a parametrized lens mass model. However, in the case of iPTF16geu, also in the case of a very flat halo with $\eta = 1.2$, the central image would be below our detection limit, even when ignoring dust extinction.

5.2 Lens mass constraints from imaging data

In order to constrain also the slope of the deflector, we include full imaging data using `lenstronomy`, an open-source PYTHON package using forward modelling to reconstruct strong lensing systems (Birrer & Amara 2018). We simultaneously reconstruct the lens mass model, the SN images (when applicable) and the surface brightness distributions of the lens and the lensed iPTF16geu host galaxy. Compared to systems of strongly lensed quasars, we can take advantage of the fact that the transient nature of SNe allows for accurate reference imaging, i.e. we have a clear view of the lensed host when the SN has faded.

The lens mass is described by equation (19), using zero core size, $s = 0$. For the lens galaxy and (unlensed) host galaxy light intensity, we assume elliptical Sérsic profiles:

$$I(R) = I_e \exp \left[-b_n \left(\frac{R}{R_e} \right)^{1/n} - 1 \right], \quad (26)$$

²In fact, it is not possible to successfully reproduce the observed iPTF16geu fluxes with the employed lens model, even when allowing for varying slope and core size, η and s , respectively.

where I_e is the intensity at the half-light radius R_e , $b_n = 1.9992n - 0.3271$ (Birrer & Amara 2018), and

$$R \equiv \sqrt{x_1^2 + x_2^2/q_s^2}, \quad (27)$$

where x_1 and x_2 are coordinates aligned with the major and minor axes of the galaxy light distribution, and q_s is the axial ratio.

5.2.1 HST imaging data

We expect to get the most reliable and conservative results from the lens modeling from *HST* data, given the relatively well-known and stable point spread functions (PSFs), determined empirically in appendix B of Dhawan et al. (2020). However, due to their limited resolution, compared to the size of the lens system, *HST* data may not be very effective in constraining the slope η of the lens mass distribution. Out of the available *HST* filters, we concentrate on *F814W* data, being least subject to dust extinction and displaying the most evident separation between the SN, the lens galaxy, and the host galaxy fluxes.

Minimizing the residual difference between the observed and the model image for a range of lens mass slopes in the interval $1.2 < \eta < 2.5$, we find that the *F814W* data only provide an upper limit of $\eta \lesssim 1.7$ at 95 per cent CL, in contrast to previous work in which the slope was constrained to $\eta = 2.1 \pm 0.1$ (More et al. 2017). The best-fitting model, for which $\eta = 1.2$ has a reduced chi-square of $\chi_v^2 = 0.99735$. Low values for η are also preferred by *F814W* reference imaging after iPTF16geu had faded, although the overall quality of the fit is somewhat decreased compared to the imaging when iPTF16geu was active. We note that a possible reason for this, and also for the slightly discrepant value of η compared to constraints from Keck imaging, velocity dispersion measurements, and iPTF16geu image magnifications discussed in upcoming sections, is that the host images are affected by dust absorption as evident from the iPTF16geu images. Also, fig. 3 in Johansson et al. (2020) shows evidence of colour gradients in the host galaxy along the Einstein ring, possibly related to lens galaxy dust extinction. Given the longer integration time of the *HST* reference images, the noise level is decreased, and the sensitivity to not correcting the host galaxy images for the differential dust extinction (which is beyond the scope of this paper) is increased.

5.2.2 Keck imaging data

Since constraining the slope relies on high spatial resolution data, preferably at long wavelengths in order to minimize sensitivity to dust extinction, we also investigate to what extent Keck host imaging data can provide additional information about the lens mass distribution. The Keck LGS-AO PSF may vary substantially both in time and over the focal plane, potentially making the lens modelling less reliable than for *HST* data, despite the higher resolution of the Keck LGS-AO data. Since iPTF16geu and reference imaging in the *H* band were obtained with different instruments, and conditions during K_s observations were unstable, we will use data obtained in the *J* band, having the highest quality out of the three Keck bands.

We approximate the PSF as a Moffat profile being constant in time and space. Since there are no isolated stars in the field, we determine its parameters from the SN images, after subtracting the reference image. We then model the lens mass distribution from the reference image of the lensed host galaxy, since we expect this to be less sensitive to the exact shape of the PSF, compared to imaging when

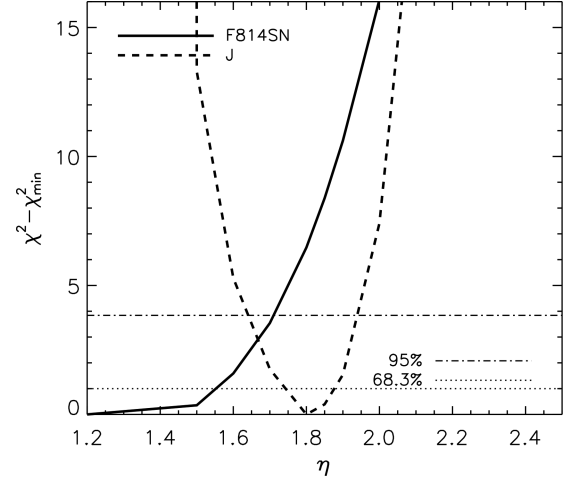


Figure 1. The χ^2 obtained from modelling the iPTF16geu system using observations in the *HST F814W* band when the SN was active (F814SN, solid line) and Keck *J*-band reference imaging (J, dashed line) as a function of the lens mass slope η . The horizontal dotted and dash-dotted lines indicate 68.3 and 95 per cent CL, respectively. *F814W* data indicate $\eta < 1.7$, whereas *J* data give $\eta = 1.8 \pm 0.15$ at 95 per cent CL.

iPTF16geu is active. The lens model parameters obtained are consistent with that from *HST* data, except that it favours a slightly higher slope of $\eta = 1.8 \pm 0.15$ at 95 per cent CL; see Fig. 1. Adding information on the iPTF16geu image positions, when fitting the *J*-band image slightly shifts the best-fitting value of the slope to $\eta \sim 1.7$.

Summarizing, there is a slight tension between the lens mass slope best fitting the *HST* and Keck data. One reason could be that the assumed mass and light distribution models are too restrictive, and another that the tension is caused by incomplete descriptions of the image PSFs. Also, given the large extinction evident in the iPTF16geu images, we can not rule out the possibility that the *HST* host images are affected by dust extinction, not corrected for in the present analysis. In the next section, we investigate how the slope can be independently constrained using the observed magnifications of the iPTF16geu images.

Figs 2 and 3 show the observed and reconstructed *HST F814W*-band and Keck *J*-band image for $\eta = 1.8$ (for reasons that will soon become evident). We obtain very similar results for lower values of η , the only exception being that the intrinsic size and luminosity of the host galaxy becomes smaller since the magnification increases as η decreases. From the left- to right-hand side, the upper panel shows the reconstructed lens galaxy light distribution, the unlensed host, and the lensed host image. In the lower panel, the observed image is shown to the left-hand side and the total reconstructed image in the middle, i.e. the sum of the lens and the lensed host light intensity. The reconstructed images have been convolved with the PSF of the instrument, but do not include the background or Poisson noise. To the right-hand side, normalized residuals after subtracting the reconstructed (model) image and the observed image (data) are shown.

6 MACROLENS VELOCITY DISPERSION MODELLING

An independent velocity dispersion measurement of the lensing galaxy can be used to break the mass sheet degeneracy, and to constrain the slope of the lens mass distribution. Johansson et al. (2020) present high-resolution spectroscopic observations of iPTF16geu, and derive a velocity dispersion of the lens galaxy,

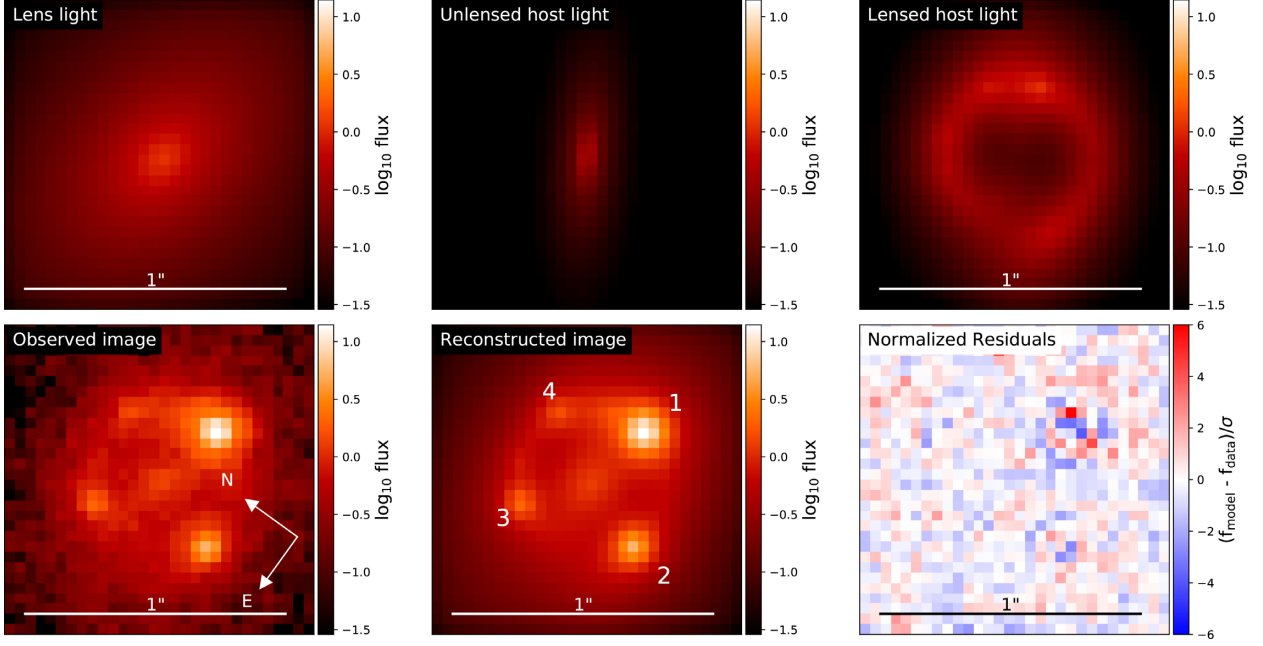


Figure 2. A comparison between the observed (data) image and the reconstructed (model) image for the *HST* *F814W*-band as of 2016 October 25, assuming a lens mass slope of $\eta = 1.8$. Upper panel from the left- to right-hand side: the reconstructed lens galaxy light intensity, the unlensed host, and the lensed host image. Lower panel from the left- to right-hand side: the observed *F814W*-band image, the total reconstructed image (convolved with the PSF of the instrument, but without background or Poisson noise), and normalized residuals. As indicated by the compass in the lower left-hand panel, the images are rotated with respect to the Keck *J*-band image in Figs 3 and 8. In the lower middle panel, the iPTF16geu images are labelled according to the numbering given in Table 1.

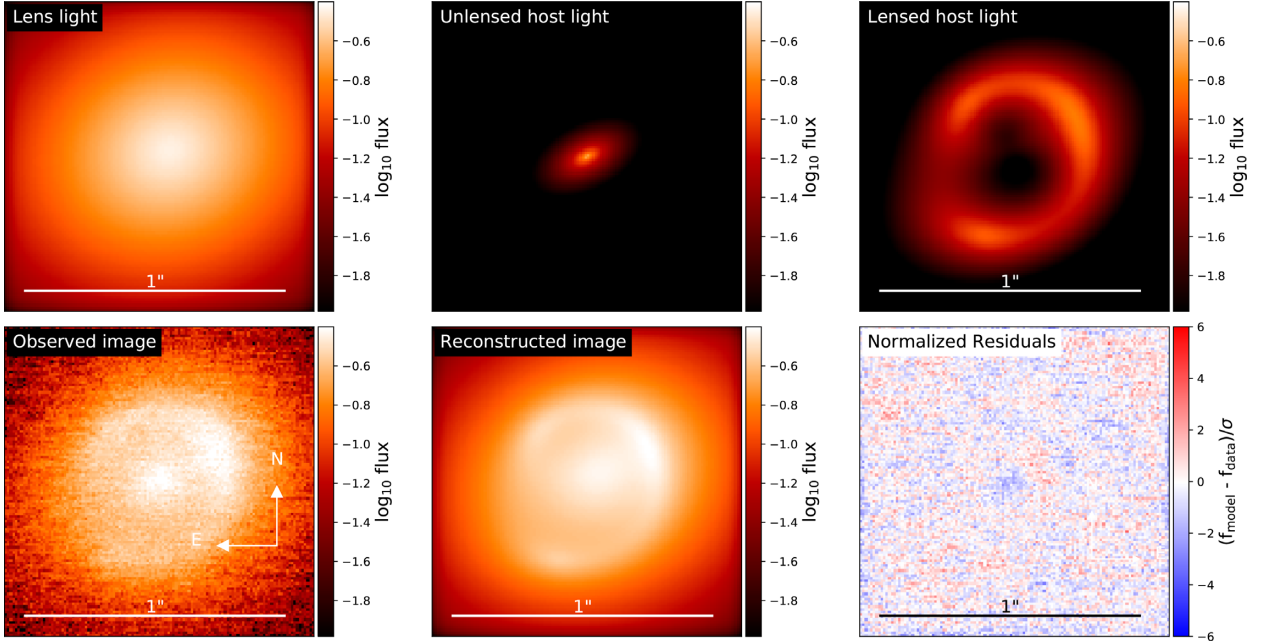


Figure 3. A comparison between the observed (data) image and the reconstructed (model) image for the Keck *J*-band reference image as of 2017 June 16, assuming a lens mass slope of $\eta = 1.8$. Upper panel from the left- to right-hand side: the reconstructed lens galaxy light intensity, the unlensed host, and the lensed host image. Lower panel from the left- to right-hand side: the observed *J*-band image, the total reconstructed image (convolved with the PSF of the instrument, but without background or Poisson noise), and normalized residuals.

$\sigma_{\text{obs}} = 129 \pm 4 \text{ km s}^{-1}$, using stellar continuum fitting. This value is lower, but consistent with the value derived from emission lines in low-resolution spectra, $\sigma_{\text{obs}} = 163_{-27}^{+41} \text{ km s}^{-1}$ (Goobar et al. 2017).

The theoretical velocity dispersion for a spherically symmetric system can be derived from the equations of stellar hydrodynamics:

$$\frac{d}{dr} (v\sigma_r^2) + \frac{2\beta}{r} v\sigma_r^2 = -v \frac{d\Phi}{dr} \equiv -v\Phi', \quad (28)$$

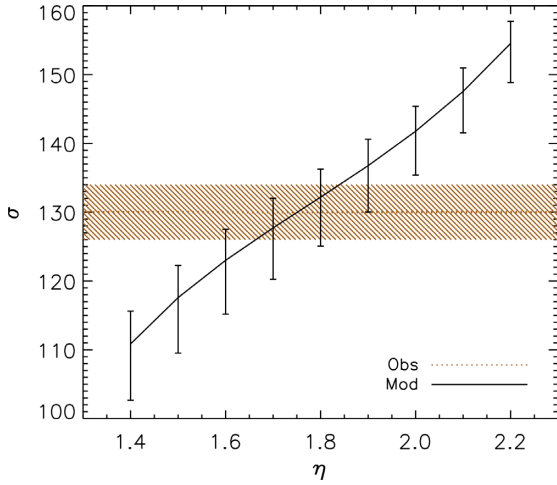


Figure 4. The predicted lens galaxy velocity dispersion as a function of the lens mass slope η . The value $\eta = 2$ represents an isothermal halo. The horizontal bands indicate the observed velocity dispersion of $\sigma_{\text{obs}} = 129 \pm 4 \text{ km s}^{-1}$ (Johansson et al. 2020), favouring values for the slope in the interval $1.6 < \eta < 2$.

where σ_t and σ_r are the velocity dispersions in the tangential and radial direction, respectively, $\beta = 1 - (\sigma_t/\sigma_r)^2$ is the velocity anisotropy, ν is the three-dimensional density of velocity dispersion tracers (luminous matter), and Φ is the total gravitational potential. The prime indicates differentiation with respect to r . Assuming constant β ,

$$\sigma_r^2(r) = \frac{1}{\nu r^{2\beta}} \int_r^\infty \nu x^{2\beta} \Phi' dx. \quad (29)$$

To estimate the expected velocity dispersion of the iPTF16geu lens galaxy, we approximate the light and mass distributions as spherically symmetric and deproject the best-fitting Sérsic profile for the lens luminosity distribution and the power-law-projected total mass profile to obtain $\nu(r)$ and $\Phi(r)$, respectively.³

The lens luminosity distribution is derived from *HST* *F475W*, expected to most closely trace the star distribution used when observationally constraining the velocity dispersion; see Johansson et al. (2020). In doing this, we keep the lens mass distribution obtained from *F814W* data fixed. The model velocity dispersion, σ_{mod} , is given by a line-of-sight luminosity-weighted average over the effective spectroscopic aperture of the observations, here approximated as a circular aperture with radius 0.9 arcsec. In Fig. 4, we show σ_{mod} as a function of lens mass slope η . Compared with the observed velocity dispersion of $\sigma_{\text{obs}} = 129 \pm 4 \text{ km s}^{-1}$, indicated by the horizontal band, we see that $1.6 < \eta < 2$ are preferred, in reassuring agreement with the values obtained from the iPTF16geu image fluxes in Section 8.3. The main uncertainty is the anisotropy parameter, β , for which we conservatively assume $\beta = 0.2_{-0.5}^{+0.2}$ (Gerhard et al. 2001; Chae, Bernardi & Sheth 2019), yielding $\sigma_{\text{mod}} = 132_{-7}^{+4} \text{ km s}^{-1}$ for $\eta = 1.8$.

³We have used codes developed by Matthew Auger and Alessandro Sonnenfeld; available at https://github.com/astrosonnen/spherical_jeans.

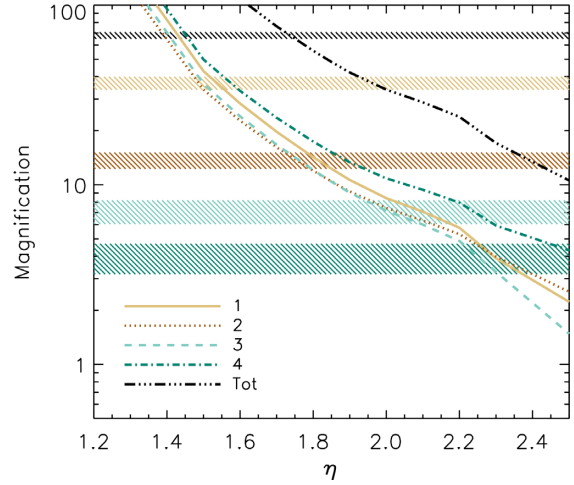


Figure 5. The predicted magnifications for the iPTF16geu images 1–4 and their total magnification, as a function of the lens mass slope η . The value $\eta = 2$ represents an isothermal halo. The horizontal bands indicate the observed magnifications listed in Table 1. The predicted magnifications decrease monotonically with η . In contrast to the observed values, the models always predict similar magnifications for all four images, with image 4 being the brightest.

7 MACROLENS IMAGE MAGNIFICATIONS MODELLING

Since the inferred value of the *Hubble* constant depends directly on the slope of the projected lens mass η , and smaller η implies larger image magnifications, in this section, we take advantage of the standard candle nature of SNe Ia observationally constraining the image magnifications as listed in Table 1, in order to resolve the tension between the inferred slope from *HST* and Keck data. In Fig. 5, the predicted magnifications for the individual iPTF16geu images as a function of the slope η , as well as the total magnification, are plotted together with the observed values indicated by the horizontal bands. Two things are immediately apparent: Ignoring substructure lensing effects, the observed total magnification suggests that $\eta \sim 1.75$ [(close to the value preferred by Keck data (see Fig. 1), and velocity dispersion observations (see Fig. 4)]; Also, regardless of the value of η , a smooth lens density fails to explain the individual iPTF16geu image fluxes, and additional substructure lensing is needed. This is the subject of the upcoming section.

8 MICROLENS MODELLING

In order to use the iPTF16geu image magnifications when modelling the macrolens mass distribution, we also have to take into the fact that substructure in the form of, for example, stars in the lens galaxy may give rise to additional (de)magnification of the iPTF16geu images.

8.1 Stellar microlensing

Lens galaxy stars can microlens strongly lensed compact sources, such as quasars or SNe, significantly altering their observed fluxes (Chang & Refsdal 1979). Although the principles of microlensing are the same as those of galaxy-scale strong gravitational lensing (see Section 2), there are some important differences between the two scenarios. First, the significantly lower deflector masses involved in microlensing ($m \sim M_\odot$) lead to microimage time delays

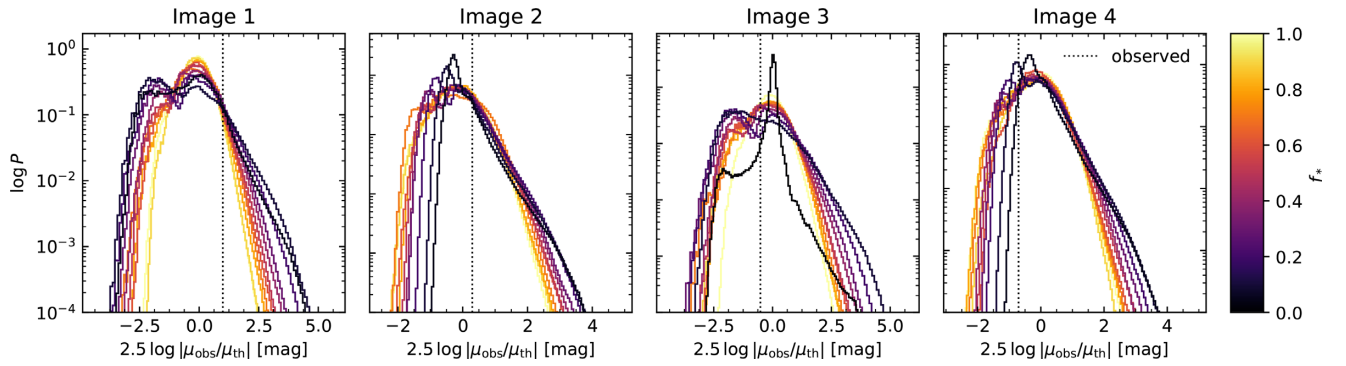


Figure 6. Microlensing magnification PDFs for each image of iPTF16geu. Histograms show the distribution of differences, in magnitudes, between the total magnification of each image, μ_{tot} , and the magnification predicted from a smooth model, μ_{th} . The required microlensing magnifications as derived from the observed image fluxes are indicated by vertical dotted lines. f_* denotes the fraction of matter in stars at the location of each image.

and image separations that are too small to be observed with current optical instrumentation (typically of the order of 10^{-6} s and 10^{-6} arcsec, respectively; Moore & Hewitt 1996). Secondly, individual deflectors are replaced by fields of lens stars, having complex caustic patterns that vary over spatial scales of microarcseconds. These patterns can magnify or demagnify compact sources by several magnitudes over the value expected from a smooth lens model (e.g. Kayser, Refsdal & Stabell 1986; Schneider & Weiss 1987; Wambsganss 1992). This effect has been observed in many lensed quasars (e.g. Irwin et al. 1989; Witt, Mao & Schechter 1995; Tewes, Courbin & Meylan 2013), and simulations indicate that it should be ubiquitous in the multiple images of strongly SNe (Dobler & Keeton 2006; Goldstein et al. 2018).

To determine if microlensing can explain the flux anomalies in iPTF16geu, we use a set of publicly available microlensing magnification patterns produced by the GERLUMPH project (Vernardos et al. 2014). The maps were generated by the inverse ray-shooting method (Wambsganss 1999), in which a uniform surface density of rays is followed from the observer through a random field of point-mass deflectors in the lens galaxy, and collected in pixels on the source plane. The ray count in each pixel is proportional to the lensing magnification that a source at the position of the pixel would experience.

The statistical properties of the microlensing are determined by the macrolensing model convergence and shear, κ and γ , as well as the fraction of matter in stars, f_* , at the location of each image. For our best-fitting lens mass models, images 1 and 3 correspond to saddle points of the time delay surface in equation (2) (for which $\det \mathcal{A} < 0$) and images 2 and 4 to minima (for which $\det \mathcal{A} > 0$ and $\text{Tr} \mathcal{A} > 0$). In the simulations, fields of stars were realized at the location of each image by assuming a uniform deflector mass $m = M_{\odot}$ (Vernardos et al. 2014). Studies of lens galaxy star fields have established that $m = 0.3 M_{\odot}$ is a more representative value (Poindexter & Kochanek 2010), but other studies indicate that the deflector mass has a negligible effect on the microlensing magnification probability distributions (Wambsganss 1992; Lewis & Irwin 1995; Wytke & Turner 2001; Schechter, Wambsganss & Lewis 2004).

8.2 Stellar mass fractions

With the knowledge of stellar mass-to-light ratios, m/L , we can estimate the stellar mass surface density at the iPTF16geu image positions from the lens light intensity. Combined with the total

Table 3. Stellar mass fractions, f_* , at the iPTF16geu image positions as derived from *HST* F814W photometry approximated by the SDSS *i*-band and lens modelling, assuming a lens mass slope $\eta = 1.8$.

Image	f_* (5%)	f_* (25%)	f_* (50%)	f_* (75%)	f_* (95%)
1	0.073	0.130	0.198	0.271	0.422
2	0.069	0.122	0.186	0.256	0.397
3	0.065	0.115	0.175	0.241	0.373
4	0.067	0.118	0.180	0.247	0.384

Note. The columns correspond to 5th, 25th, 50th (median), 75th, and 95th percentile mass fractions.

surface mass density as derived from the lens modelling, we obtain the stellar mass fraction, f_* , needed to determine the stellar microlensing probabilities for the SN images. In Kauffmann et al. (2003), m/L as a function of the host galaxy magnitude are presented for four out of the five Sloan Digital Sky Survey (SDSS) band, namely *g*, *r*, *i*, and *z*. Since the scatter in m/L decreases at longer wavelengths, we use lens galaxy imaging in the *HST* F814W band, which overlaps to large extent with the SDSS *i* band. The lens light distribution is derived using the parametric fit described in Dhawan et al. (2020).

The absolute magnitude of the lens galaxy is *k*-corrected to the *i* band at a redshift of $z = 0.1$ is $M_i = -20.4$. Using fig. 14 in Kauffmann et al. (2003) gives a median $(m/L)_i = 1.70$ in solar units for which the absolute magnitude is $M_{\odot,i} = 4.58$ at $z = 0.1$. The 5th, 25th, 75th, and 95th percentile mass-to-light ratios are given by $(m/L)_i = [0.63, 1.12, 2.34, 3.63]$. The corresponding stellar mass fractions, f_* , at the SN image positions for $\eta = 1.8$ (with similar results for other values of η) are presented in Table 3.

8.3 Stellar microlensing probabilities

In Fig. 6, we show the microlensing magnification probability density functions (PDFs) for each image, assuming a slope of $\eta = 1.8$. Here, μ_{tot} is the total magnification of each image and μ_{th} the (absolute value of the) smooth lens model magnification. Thanks to the standard candle nature of SNe Ia, the required microlensing magnification can be estimated (vertical dotted lines) and compared to the microlensing PDFs, assuming different values of η . The probability for each image is obtained by taking a weighted average of the one-tailed *p*-value for the corresponding f_* (listed in Table 3 for the case of $\eta = 1.8$). The total probability, p_{tot} , for stellar microlensing to explain the observed iPTF16geu image fluxes is

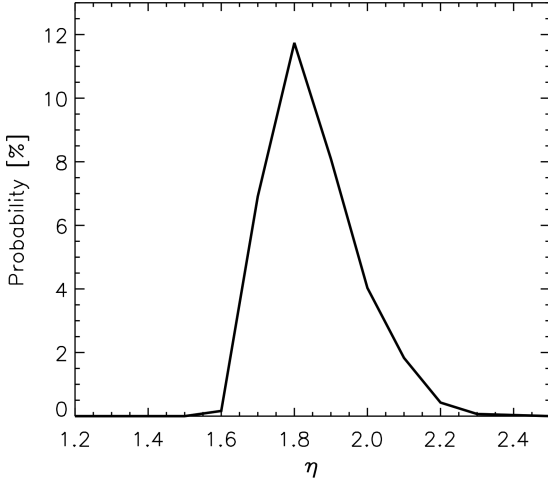


Figure 7. The probability for stellar microlensing to explain the observed iPTF16geu image fluxes as a function of the lens mass slope η , calculated in steps of $\Delta\eta = 0.1$. The probability is maximized at 12 percent for $\eta = 1.8$.

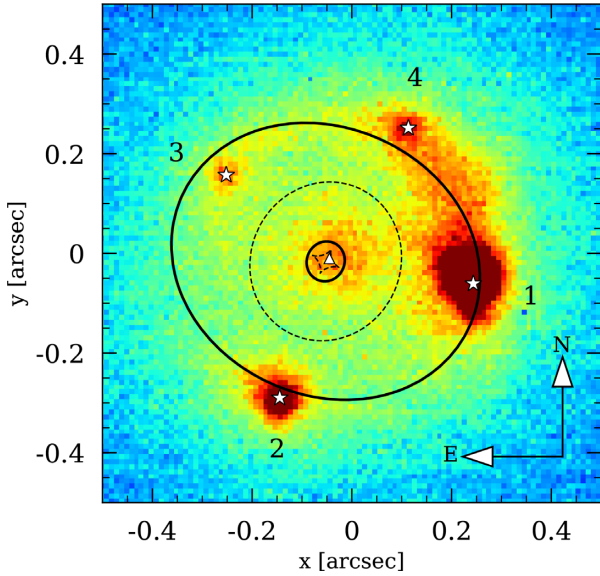


Figure 8. Critical curves (solid black) and caustics (dotted black) for the best-fitting lens model assuming $\eta = 1.8$ overlaid on Keck LGS-AO J -band imaging data. The white asterisks denote iPTF16geu images positions, labelled by their number in Table 1 (Goobar et al. 2017), and the white triangles denote the source position.

obtained by combining the individual image probabilities using the Fisher’s combined probability test (Fisher 1925). As shown in Fig. 7, this probability is maximized for $\eta = 1.8$, yielding $p_{\text{tot}} = 0.12$, primarily driven by the large microlensing magnification required for image 1. In Table 4, we list the convergence κ , the shear γ , the (signed) smooth lens model magnification μ_{th} , the observed magnifications μ_{obs} , and the probability p for stellar microlensing to accommodate the difference between μ_{th} and μ_{obs} for the case of $\eta = 1.8$. We note that the probability derived is higher than that obtained in Yahalomi et al. (2017). This can be attributed to the difference in the assumed slope of the lens mass distributions, our updated magnifications factors taking dust extinction into account, and differences in the way the individual probabilities for each

Table 4. For each image, the convergence κ , the shear γ , and the (signed) magnification predicted for a smooth halo μ_{th} , assuming a lens mass slope of $\eta = 1.8$, are listed, together with the one-tailed p -values, derived from the microlensing PDFs shown in Fig. 6 using stellar mass fractions, f_* , listed in Table 3.

Image	κ	γ	μ_{th}	p
1	0.644 ± 0.004	0.444 ± 0.004	$-14.2^{+1.1}_{-1.3}$	0.08
2	0.546 ± 0.004	0.349 ± 0.004	$11.9^{+0.9}_{-0.7}$	0.21
3	0.653 ± 0.005	0.451 ± 0.005	$-12.0^{+1.0}_{-1.2}$	0.43
4	0.566 ± 0.003	0.362 ± 0.003	$17.4^{+1.5}_{-1.2}$	0.22

Note. The total probability for the observed magnifications is $p_{\text{tot}} = 0.12$.

image are combined. We conclude that stellar microlensing, with an acceptable level of probability, can explain the observed flux anomalies for iPTF16geu. Note that the use of microlensing to place constraints on the macrolens model is only possible since the source is a precisely calibrated standard candle.

9 LENS MODEL AND HUBBLE CONSTANT RESULTS

In this section, we summarize the results on the lens mass distribution, and derive limits on the *Hubble* constant using the observed time delay between the iPTF16geu images.

9.1 Lens model parameters

Given the constraint on the lens mass slope derived from the iPTF16geu image magnifications and velocity dispersion observations, strengthened by their agreement with LGS-AO Keck data, in the following, we assume a value of $\eta = 1.8$. In Table 5, we present the resulting lens mass distribution parameters as derived from *HST* $F814W$ data, and Keck J reference imaging. The two independent fits display a reassuring agreement, the only notable difference being that Keck data indicate a slightly higher ellipticity of the lens mass distribution.

Fig. 8 shows the critical curves, corresponding to image positions with infinite magnification, i.e. $\det \mathcal{A}(\theta) = 0$, and caustics, the corresponding source positions, for the best-fitting lens model with slope $\eta = 1.8$ overlaid on Keck LGS-AO J -band imaging data.

Given the high degree of circular symmetry of the lens system, the ellipticity of the lensing galaxy is degenerate with a possible external shear component for light deflections close to the critical curve. If the external shear is caused by a SIS galaxy, its magnitude is given by

$$\gamma_{\text{ext}} = \frac{b_{\text{ext}}}{2r} = \frac{2\pi\sigma_v^2}{r} \left(\frac{D_{\text{ls}}}{1157 \text{ Mpc}} \right), \quad (30)$$

where b_{ext} is the Einstein radius of the external perturber, r the projected distance between the lensing galaxies, and σ_v the velocity dispersion of the perturber. The largest expected contribution from galaxies in a square field with side length 100 arcsec centred on the iPTF16geu system is from a galaxy with $r \approx 58$ arcsec at $\phi \approx 40^\circ$ and an SDSS photometric redshift estimate of $z = 0.336 \pm 0.0365$ (Blanton et al. 2017). From its g -band magnitude of $m_g = 20.77$, we can estimate its velocity dispersion to $\sigma_v \approx 187 \text{ km s}^{-1}$ (Mitchell et al. 2005; Jönsson et al. 2008). This corresponds to a shear contribution of $\gamma_{\text{ext}} = 1.4 \times 10^{-4}$ for iPTF16geu. Other individual galaxies in the field contribute at most 20 percent of this value

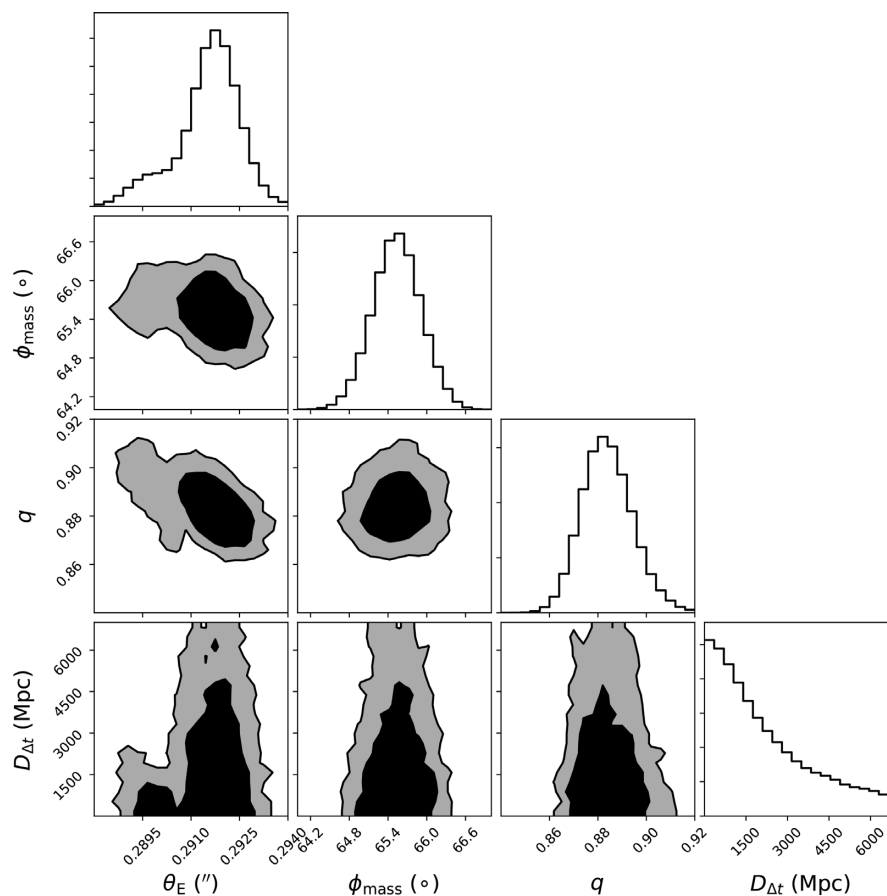


Figure 9. Confidence contours for the time delay distance $D_{\Delta t}$, together with the lens mass parameters θ_E , ϕ_{mass} , and q , derived from *HST* F814W data, assuming a lens mass slope of $\eta = 1.8$. The corresponding limits on the *Hubble* constant are $h > 0.5$ and $h > 0.2$, at 68.3 and 95 per cent CL, respectively.

Table 5. Derived parameters for the lens mass distribution of the iPTF16geu system, assuming a lens mass slope of $\eta = 1.8$ from *HST* F814W-band data when iPTF16geu is active and Keck *J*-band reference imaging.

Parameter	<i>HST</i> F814W	Keck <i>J</i>
θ_E (arcsec)	0.292 ± 0.001	0.291 ± 0.001
ϕ_{mass} ($^\circ$)	65.5 ± 0.3	65.0 ± 0.8
q	0.88 ± 0.01	0.77 ± 0.01

Note. The inclination angle ϕ_{mass} of the major axis is defined in observers’ coordinates, east of north (i.e. with respect to the y -axis in a Cartesian coordinate system).

and we conclude that the major part of the shear is caused by the ellipticity of the lensing galaxy itself.

9.2 Time delays and h

The measured time delays in Table 2 can be used to constrain the value of the time delay distance $D_{\Delta t}$, using equation (2), and finally the *Hubble* constant h . In practice, this is done using *lenstronomy* in a manner very similar to when constraining only the lens and source properties. The only difference is that we also include the time delays as observational constraints. In principle, including time delays may also change the derived lens properties. However, since in the case of iPTF16geu the time delay uncertainties are large, in practice, they will only constrain $D_{\Delta t}$.

Given the large uncertainties in $D_{\Delta t}$, we have assumed fixed (*Planck*) values for cosmological parameters other than h when translating from $D_{\Delta t}$ into h . Fig. 9, shows the confidence contours for $D_{\Delta t}$, together with the lens mass parameters θ_E , ϕ_{mass} , and q , derived from *HST* F814W data, assuming a lens mass slope of $\eta = 1.8$. Since the observed time delays are consistent with being zero at 1σ , we can only (weakly) constrain $D_{\Delta t}$ from above and, consequently, h from below to $h > 0.5$ and $h > 0.2$ at 68.3 and 95 per cent CL, respectively. Since the derived *Hubble* constant scales with the observed time delays, Δt_{ij} , and the slope of the lens mass distribution as $h \propto (\eta - 1)/\Delta t_{ij}$, conservatively assuming a very shallow lens profile with $\eta = 1.6$, the constraints are slightly weakened to $h > 0.4$ and $h > 0.15$ at 68.3 and 95 per cent CL, respectively.

As discussed in Dhawan et al. (2020), we expect to be able to decrease the uncertainty on h considerably, given a strongly lensed SN Ia observed closer to its maximum light, and with larger time delays between the images.

10 CONCLUSIONS

With the aid of follow-up observations of iPTF16geu, we derive tighter constraints on the lens model, as well as the first constraint on the *Hubble* constant from observations of a strongly lensed SN Ia, following Refsdal’s original proposal (Refsdal 1964). The projected mass distribution of the lens galaxy is determined, including the slope that is constrained by the iPTF16geu image magnifications

and velocity dispersion measurements to $\eta \sim 1.8$, flatter than an isothermal profile for which $\eta = 2$.

The fact that iPTF16geu exploded very close to the centre of the inner caustic of the lens makes the predicted images for a smooth lens to be similar, in terms of the radial position, magnification, and arrival time. Since the majority of the data is post first maximum, the measurement of the time delays between images is challenging. Combined with the fact that the absolute time delays are small, the resulting fractional uncertainties are large. We expect constraints on the *Hubble* constant to be dominated by uncertainties in the arrival time of the images and obtain a relatively weak lower limit on the current expansion rate of $h \gtrsim 0.4$ at 68.3 per cent CL.

Observational limits on the image fluxes are better constrained, and show beyond doubt that substantial additional (de)magnification from substructure, possibly stars, in the lens has to take place. Compared to macrolens predictions, images 1 and 2 need an additional magnification of $\Delta m_1 = -1.0$ and $\Delta m_2 = -0.3$, whereas images 3 and 4 require a demagnification of $\Delta m_3 = 0.5$ and $\Delta m_4 = 0.7$, possibly from substructure lensing. Estimating the stellar mass fractions at the iPTF16geu image positions, we derive stellar microlensing magnification probabilities for each image. The total probability for stellar microlensing to explain the observed flux anomalies is $p_{\text{tot}} \sim 12$ per cent. We conclude that the iPTF16geu flux ‘anomalies’ are within stellar microlensing predictions. This is the first time that microlensing has been used in combination with a precisely calibrated standard candle to place constraints on the macrolens model in a strong lensing system.

ACKNOWLEDGEMENTS

We thank the anonymous referee for many insightful comments helping to improve the quality of this paper. Also, thanks to Simon Birrer, Rahul Gupta, and Mattia Bulla for help in running *lenstronomy*. AG acknowledges support from the Swedish National Space Agency and the Swedish Research Council.

REFERENCES

Ade P. A. R. et al., 2016, *A&A*, 594, A13
 Aghanim N. et al., 2016, *A&A*, 596, A107
 Amanullah R., Mörtzell E., Goobar A., 2003, *A&A*, 397, 819
 Amanullah R. et al., 2011, *ApJ*, 742, L7
 Birrer S., Amara A., 2018,
 Blanton M. R. et al., 2017, *AJ*, 154, 28
 Chae K.-H., Bernardi M., Sheth R. K., 2019, *ApJ*, 874, 41
 Chang K., Refsdal S., 1979, *Nature*, 282, 561
 Chornock R. et al., 2013, *ApJ*, 767, 162
 Dhawan S., Goobar A., Mörtzell E., 2018, *J. Cosmol. Astropart. Phys.*, 1807, 024
 Dhawan S. et al., 2020, *MNRAS*, 491, 2639
 Dobler G., Keeton C. R., 2006, *ApJ*, 653, 1391
 Falco E. E., Gorenstein M. V., Shapiro I. I., 1985, *ApJ*, 289, L1
 Fisher R., 1925, *Statistical Methods for Research Workers*. Oliver & Boyd, Edinburgh
 Gerhard O., Kronawitter A., Saglia R. P., Bender R., 2001, *AJ*, 121, 1936
 Goldstein D. A., Nugent P. E., Kasen D. N., Collett T. E., 2018, *ApJ*, 855, 22
 Goliath M., Mörtzell E., 2000, *Phys. Lett.*, B486, 249
 Goobar A., Leibundgut B., 2011, *Annu. Rev. Nucl. Part. Sci.*, 61, 251
 Goobar A., Mörtzell E., Amanullah R., Nugent P., 2002, *A&A*, 393, 25
 Goobar A. et al., 2009, *A&A*, 507, 71

Goobar A. et al., 2017, *Science*, 356, 291
 Hsiao E. Y., Conley A., Howell D. A., Sullivan M., Pritchett C. J., Carlberg R. G., Nugent P. E., Phillips M. M., 2007, *ApJ*, 663, 1187
 Irwin M. J., Webster R. L., Hewett P. C., Corrigan R. T., Jedrzejewski R. I., 1989, *AJ*, 98, 1989
 Johansson J. et al., 2020, preprint ([arXiv:2004.10164](https://arxiv.org/abs/2004.10164))
 Jönsson J., Dahlén T., Goobar A., Gunnarsson C., Mörtzell E., Lee K., 2006, *ApJ*, 639, 991
 Jönsson J., Dahlén T., Goobar A., Mörtzell E., Riess A., 2007, *J. Cosmol. Astropart. Phys.*, 0706, 002
 Jönsson J., Kronborg T., Mörtzell E., Sollerman J., 2008, *A&A*, 487, 467
 Jönsson J., Mörtzell E., Sollerman J., 2009, *A&A*, 493, 331
 Jönsson J., Dahlén T., Hook I., Goobar A., Mörtzell E., 2010, *MNRAS*, 402, 526
 Kassiola A., Kovner I., 1993, in Surdej J., Fraipont-Caro D., Gosset E., Refsdal S., Remy M., eds, *Liege Int. Astrophys. Colloq. Vol. 31, Gravitational Lenses in the Universe*, Universite de Liege. Liege, p. 571
 Kauffmann G. et al., 2003, *MNRAS*, 341, 33
 Kayser R., Refsdal S., Stabell R., 1986, *A&A*, 166, 36
 Keeton C. R., 2001a, ([arXiv:astro-ph/0102340](https://arxiv.org/abs/astro-ph/0102340))
 Keeton C. R., 2001b, ([arXiv:astro-ph/0102341](https://arxiv.org/abs/astro-ph/0102341))
 Kelly P. L. et al., 2016a, *ApJ*, 819, L8
 Kelly P. L. et al., 2016b, *ApJ*, 831, 205
 Kolatt T. S., Bartelmann M., 1998, *MNRAS*, 296, 763
 Kormann R., Schneider P., Bartelmann M., 1994, *A&A*, 284, 285
 Lewis G. F., Irwin M. J., 1995, *MNRAS*, 276, 103
 Metcalf R. B., Silk J., 1999, *ApJ*, 519, L1
 Mitchell J. L., Keeton C. R., Frieman J. A., Sheth R. K., 2005, *ApJ*, 622, 81
 Moore C. B., Hewitt J. N., 1996, in Kochanek C. S., Hewitt J. N., eds, *Proc. IAU Symp. 173, Astrophysical Applications of Gravitational Lensing*. Kluwer, Dordrecht, p. 279
 More A., Suyu S. H., Oguri M., More S., Lee C.-H., 2017, *ApJ*, 835, L25
 Mörtzell E., 2002, *A&A*, 382, 787
 Mörtzell E., Dhawan S., 2018, *J. Cosmol. Astropart. Phys.*, 1809, 025
 Mörtzell E., Sunesson C., 2006, *J. Cosmol. Astropart. Phys.*, 0601, 012
 Mörtzell E., Goobar A., Bergstrom L., 2001a, *ApJ*, 559, 53
 Mörtzell E., Gunnarsson C., Goobar A., 2001b, *ApJ*, 561, 106
 Mörtzell E., Dahle H., Hannestad S., 2005, *ApJ*, 619, 733
 Nordin J. et al., 2014, *MNRAS*, 440, 2742
 Oguri M., Kawano Y., 2003, *MNRAS*, 338, L25
 Petrushevska T. et al., 2016, *A&A*, 594, A54
 Poindexter S., Kochanek C. S., 2010, *ApJ*, 712, 658
 Quimby R. M. et al., 2013, *ApJ*, 768, L20
 Rauch K. P., 1991, *ApJ*, 374, 83
 Refsdal S., 1964, *MNRAS*, 128, 307
 Riess A. G., Casertano S., Yuan W., Macri L. M., Scolnic D., 2019, ([arXiv:1903.07603](https://arxiv.org/abs/1903.07603))
 Rodney S. A. et al., 2015, *ApJ*, 811, 70
 Rubin D. et al., 2018, *ApJ*, 866, 65
 Schechter P. L., Wambsganss J., Lewis G. F., 2004, *ApJ*, 613, 77
 Schneider P., Weiss A., 1987, *A&A*, 171, 49
 Seljak U., Holz D. E., 1999, *A&A*, 351, L10
 Tewes M., Courbin F., Meylan G., 2013, *A&A*, 553, A120
 Vernardos G., Fluke C. J., Bate N. F., Croton D., 2014, *ApJS*, 211, 16
 Wambsganss J., 1992, *ApJ*, 392, 424
 Wambsganss J., 1999, *J. Comput. Appl. Math.*, 109, 353
 Witt H. J., Mao S., Schechter P. L., 1995, *ApJ*, 443, 18
 Wyithe J. S. B., Turner E. L., 2001, *MNRAS*, 320, 21
 Yahalomi D. A., Schechter P. L., Wambsganss J., 2017, ([arXiv:1711.07919](https://arxiv.org/abs/1711.07919))
 Zumalacarregui M., Seljak U., 2018, *Phys. Rev. Lett.*, 121, 141101

This paper has been typeset from a $\text{\TeX}/\text{\LaTeX}$ file prepared by the author.